Upscaling of solute plumes in periodic porous media through a trajectory based spatial Markov model

Emanuela Bianchi Janetti[a], Thomas Sherman[b], Gaël Raymond Guédon[c], Diogo Bolster[b], Giovanni Porta[a]

[a]*Dipartimento di Ingeneria Civile ed Ambientale, Politecnico di Milano, Milano, Italy*
[b]*Dept. of Civil and Environmental Engineering and Earth Sciences, University of Notre Dame, IN, USA*
[c]*Dipartimento di Energia, Politecnico di Milano, Milano, Italy*

Abstract

We propose an approach to upscale solute transport in spatially periodic porous media. Our methodology relies on pore scale information to predict large scale transport features, including explicit reconstruction of the solute plume, breakthrough curves at fixed distances, and spatial spreading transverse to the main flow direction. The proposed approach is grounded on the recently proposed trajectory-based Spatial Markov model (tSMM), which upscales transport based on information collected from advective-diffusive particle trajectories across one periodic element. In previous works, this model has been applied solely to one-dimensional transport in a single periodic pore geometry. In this work we extend the tSMM to the prediction of multi-dimensional solute plumes. This is obtained by analyzing the joint space-time probability distribution associated with discrete particles, as yielded by the tSMM. By comparing numerical results from fully resolved simulations and predictions obtained with the tSMM over a wide range of Péclet numbers, we demonstrate that the proposed approach is suitable for modeling transport

of conservative and linearly decaying solute species in a realistic pore space and showcase the applicability of the model to predict steady state solute plumes. Additionally, we evaluate the model performance as a function of numerical parameters employed in the tSMM parameterization.

Keywords: Upscaling, Porous Media, Transport, Spatial Markov Model, Transverse dispersion

1. Introduction

Solute transport in porous media is a fundamental problem across many disciplines, including subsurface geological systems and the performance optimization of engineered materials such as filtration membranes. A key challenge in this context is to obtain accurate predictions at spatial scales much larger than the ones associated with individual pores without having to resolve the physical and chemical processes taking place within complex pore spaces. This is achieved by upscaled formulations that embed pore scale features into effective parameters and therefore can be employed to predict large scale behaviors. To this end, a classical approach is resorting to a continuum-scale advection-dispersion equation (ADE) [1, 2]. In such a formulation mechanical dispersion induced by pore scale velocity gradients is modelled through a Fickian-like dispersion term, parameterized via a fourth-rank dispersivity tensor. The definition of the dispersivity tensor purely based on pore scale properties presents significant challenges. From a theoretical perspective, the solution of three closure problems is required to fully parameterize solute transport based on pore scale information through volume averaging [3]. These separate closures are necessary to isolate and char-

acterize the separate effects of diffusion and advection on transport. However, even such a detailed approach may not yield reliable predictions due to a lack of separation of scales, violating the assumptions required by the volume averaging method. In such a case, non-Fickian transport features emerge, particularly at relatively short times and distances [4, 5]. Formally, these effects can still be represented with Eulerian nonlocal (integro-differential) models. In principle these models can be derived by applying upscaling approaches, such as volume averaging, that can relate pore scale geometry and fluid velocities with the emerging transport dynamics through a set of closure differential equations [6]. However, it is often found that resorting to such approaches leads to formidable mathematical and numerical complexity [7, 8], which is associated with *i*) the numerical resolution of various closure problems and *ii*) the approximation of integro-differential equations to obtain the desired large scale outputs.

A specific problem in the context of solute transport upscaling is posed by the modeling of solute plumes, which correspond to the explicit spatial reconstruction of the solute spatial spread at a given time, or at steady state (i.e., under steady state boundary conditions, such as continuous injection). For instance, the analysis of transverse spreading and mixing of steady state solute plumes has great practical relevance in bioremediation and reactive transport scenarios at field and laboratory scales [9, 10, 11]. In these applications the target process is the spreading and mixing of a solute in the direction transverse to a steady flow field characterized by a prevalent direction. Following classical ADE-based descriptions, transport in the transverse direction is typically modeled by introducing a dispersivity parameter. This

standard definition typically considers dispersion to be uniquely proportional to advective velocity [1]. This formulation was successfully employed, for example to interpret transport and mixing in microfluidic systems characterized by relatively simple geometries [12]. However, studies performed in the last decade have demonstrated the impact of molecular diffusion on transverse dispersion through experiments and numerical simulations [10, 13, 14, 15]. Such results can be qualitatively linked with analytical and numerical studies showing that the dispersion tensor becomes asymmetric in advection-dominated scenarios [16, 17]. These studies show that full parameterization of the dispersion tensor can become a troublesome task, particularly in media characterized by a complex and multi-scale pore structure. Additional levels of complexity are introduced when reactive processes are also considered on top of pore scale advective-diffusive transport.

Over the last decade it has been recognized that pore-to-continuum upscaling of solute transport can often be conveniently obtained by considering solute velocities (or associated travel times) over fixed spatial increments by means of a Markov chain. This led to the formulation of various flavours of so-called Spatial Markov models [e.g. 18, 19, 20, 21]. The SMM is based on the calculation of the travel time across a fixed distance and a one step correlation existing between successive travel times. By including correlation the SMM is able to employ information available on a limited portion of the system to predict transport across much larger distances. Notably such an approach is effective in the presence of advection-dominated scenarios that become challenging to upscale with classical Eulerian approaches. The advantages of employing a spatial Markov approach to obtain the solute

breakthrough curve (or first passage time) at a given longitudinal distance has been demonstrated in a number of previous works, relying on both numerical and laboratory scale experimental datasets [e.g. 18, 21, 22, 23]. Several recent works have discussed methodologies that employ Lagrangian SMM-like approaches to predict solute particles' space-time locations at various scales of observations [24, 25]. Yet, to the best of our knowledge, this approach has not been applied to the explicit space-time reconstruction of solute plumes starting from pore scale properties. In this work we present a methodology to upscale transport of solute plumes in the longitudinal and transverse direction via a SMM. We consider periodic media, which are routinely considered as model porous media in theoretical approaches and are employed in engineering systems across a wide range of applications [26, 27, 28, 29]. Our work starts from a recently proposed trajectory-based SMM (here labelled tSMM) to upscale transport, mixing and surface reactions across porous media made up of periodic elements [30, 31]. To date, the tSMM has been constrained to a highly idealized setting, a periodic wavy channel, which while it displays some characteristics of real porous media cannot represent their full complexity, such as transverse flow or complex pore size distributions. Building on this, we analyze longitudinal and transverse transport within a realistic two-dimensional porous domain. Briefly, the specific objectives of this contribution are to *i*) extend the tSMM to the case of a multi-dimensional unsteady solute transport and *ii*) yield an efficient and accurate representation of transient and steady state solute plumes in porous media based on the multi-dimensional tSMM. This second goal entails a specific methodological challenge, as steady state plumes are typically computationally expensive to

simulate with Lagrangian particle-based approaches. Our objective is the development of an upscaled, parsimonious and computationally affordable particle-based model for this specific configuration.

2. Methodology

2.1. Pore scale setting

We consider transport of a passive solute in a periodic two-dimensional porous medium. The medium is composed of a collection of periodic unit cells, whose geometry is represented in Figure 1. The unit cell is artificially created using a stochastic generation procedure as detailed in [21, 32, 33]. The cell properties are reported in Table 1. We assume here to deal with

Porosity	L_x [m]	L_y [m]	Δ [m]	ℓ_S [m]
0.631	4.096×10^{-3}	4.096×10^{-3}	2×10^{-6}	1×10^{-4}

Table 1: Geometrical characteristics of the unit cell

a semi-infinite periodic porous domain, i.e. $x \in [0, \infty)$ and $y \in (-\infty, +\infty)$. Because the medium is composed by an infinite number of identical cells, for convenience we define

$$\hat{x} = x - L_x \text{floor}\left(\frac{x}{L_x}\right), \quad \hat{y} = y + \frac{L_y}{2} - L_y \text{floor}\left(\frac{y}{L_y} + \frac{1}{2}\right) \tag{1}$$

as a coordinate system referenced to the unit cell, $\hat{x} \in [0, L_x]$ and $\hat{y} \in [0, L_y]$, where L_x and L_y define the dimensions of the unit cell in the x- and y-directions, respectively. The cell is discretized into square pixels of side $\Delta = 2 \times 10^{-6}$ m, which for our example results in a unit cell composed of 2048×2048 pixels. The solid and fluid phases are identified by an indicator

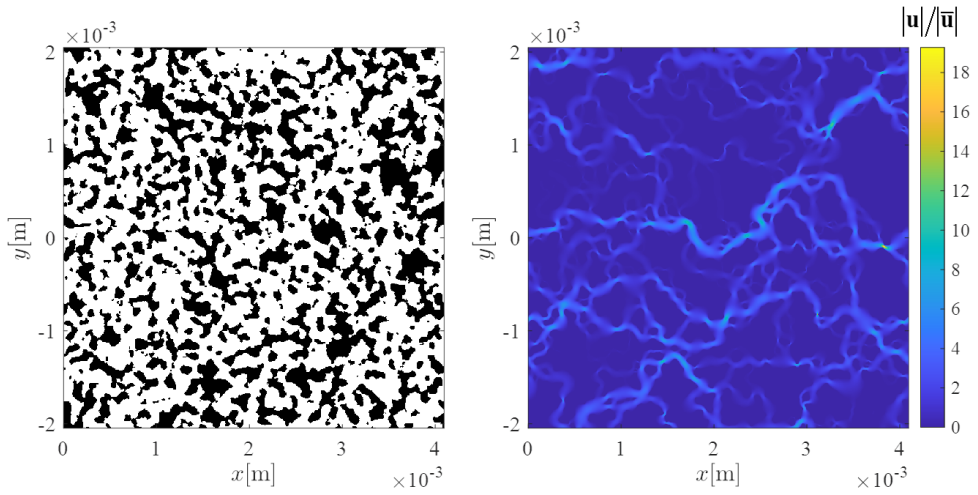

Figure 1: Geometry (left) and normalized velocity magnitude $|\mathbf{u}|/\overline{|\mathbf{u}|}$ (right) in the unit cell.

field I, with $I = 1$ associated with pore space and $I = 0$ with solid pixels. The correlation length of the indicator field I is taken as a representative length scale for the pore space and is denoted as ℓ_S. Transport is described by the standard advection-diffusion equation with no flux boundary conditions at the solid-fluid interface

$$\begin{aligned} \frac{\partial C(\mathbf{x},t)}{\partial t} + \boldsymbol{\nabla}\cdot\Big[\mathbf{u}(\mathbf{x})C(\mathbf{x},t)\Big] &= \boldsymbol{\nabla}\cdot\Big[D\boldsymbol{\nabla}C(\mathbf{x},t)\Big] \qquad \forall\,\mathbf{x}\in\Gamma_{fluid}, t>t_0 \\ D\frac{\partial C(\mathbf{x},t)}{\partial n} &= 0 \qquad \forall\,\mathbf{x}\in\Sigma_{surface}, t>t_0 \\ C(\mathbf{x},t_0) &= C_0 \end{aligned} \tag{2}$$

where $\mathbf{u} = [u, v]$ is the fluid velocity, C is solute concentration, D is the diffusion coefficient, C_0 is the initial concentration distribution. The velocity $\mathbf{u}$ is obtained by numerically solving the Navier-Stokes equations with

OpenFOAM®, release v1712 [34] and diffusion is assumed to be known and constant. The velocity is computed assuming periodic boundary conditions on the cell boundaries and the no slip condition on the fluid-solid interface. We impose a uniform pressure gradient along the x-direction, labeling x, y as longitudinal and transverse directions, respectively. The Péclet number associated with transport is calculated as $Pe = U\ell_S/D$, where U is the average fluid velocity. In our simulation we set $D = 10^{-9}$ m^2/s and we adjust Pe by setting U to the desired value. Note that this is acceptable as our simulations are in a Stokes regime, where inertial effects are negligible with respect to viscous ones. Transport is solved numerically using a Lagrangian particle based random walk method, where the solute plume is discretized into a finite number of N particles. Each particle displaces according to

$$\begin{aligned} x_i^{n+1} &= x_i^n + u_i dt + \xi_i\sqrt{2Ddt} \\ y_i^{n+1} &= y_i^n + v_i dt + \eta_i\sqrt{2Ddt} \end{aligned} \qquad i = 1, ..., N \ , \tag{3}$$

where dt is a time step that is constant, ξ_i, η_i are independent identically distributed random numbers drawn from normal distributions with zero mean and unit variance. We define a reference time step dt^* according to the following criterion $|\mathbf{d}_{max}| \leq 0.5\Delta$ where

$$|\mathbf{d}_{max}| = \max\left(|\mathbf{u}|\right) dt + 2\sqrt{2Ddt^*} \tag{4}$$

is an estimate of the maximum displacement. No flux boundary conditions at the fluid-solid boundary are imposed as elastic reflections.

2.2. Spatial Markov Model

We upscale transport using the framework of the trajectory-based spatial Markov model proposed in [30]. The methodology is based upon pore scale transport trajectories and their associated travel times. In the following, we first describe the pore scale trajectories simulations and then how these are used to parameterize the tSMM.

2.2.1. Pore scale trajectories

Parameterization of the model is grounded on the pore scale simulation of a set $S = \{s_1, \ldots, s_{N_s}\}$ of N_s advective-diffusive trajectories, for a specific Pe. These particle trajectories are simulated by solving Eq. (3) across a single cell in the longitudinal direction, i.e., between the inlet location $x = 0$ and the outlet location $x = L_x$. Figure 2 represents a sample of 100 trajectories across the considered unit cell selected from a flux weighted initial condition and setting initial location of particles distributed along the entire unit cell cross section.

For each trajectory s_i we record the travel time τ needed to travel across a distance L_x in the longitudinal direction and the y positions (y_{in}, y_{out}) of the particle at the inlet and outlet as the particle enters and exits the domain. Particles are injected at locations $x = 0, y_{in} \in [-L_y/2, L_y/2]$. Particles may cross into adjacent cells along the y direction, but due to the periodicity of the cell geometry each location y_{out} can be mapped to a corresponding $\hat{y}_{out}$ using Eq. (1). Therefore, the coordinate $y_{out}(s_i)$ can be determined as $y_{out}(s_i) = \hat{y}_{out}(s_i) + \Delta_C(s_i)L_y$ where $\Delta_C(s_i)$ is an integer that indicates the net number of cell transitions in the transverse direction observed for a given s_i trajectory path. We can then compute $\Delta y(s_i) = y_{out}(s_i) - y_{in}(s_i)$. The

trajectories are subdivided into N_B equiprobable bins that are assigned by considering the starting locations $y_{in}(s_i)$ in ascending order. This implicitly defines a discretization of the $\hat{y}$ axis in terms of the binning of the trajectories. To exemplify this binning, the trajectories in Figure 2 are subdivided into 10 bins, indicated by different colours. The trajectories s_i consider all simulated pathways between the locations $x = 0, y_{in} \in [-L/2, L_y/2]$ and $x = L_x, y_{out} \in (-\infty, +\infty)$. We observe that some trajectories may even travel backwards along x close to the inlet section before traveling downstream, as indicated in the highlighted parts in Figure 2. These effects are due to the combined action of advection and diffusion and are present for both the considered Pe. The comparison between the two considered cases allows for identification of the effects of diffusion on the pore scale trajectory paths. In particular, for $Pe = 100$ particles explore a wider portion of the pore space than for $Pe = 1000$.

2.2.2. The tSMM parameterization

The information collected in the parameterization step is then used to build the following trajectory-based Spatial Markov model (tSMM)

$$
\begin{aligned}
x_i^{k+1} &= (k+1)L_x \\
y_i^{k+1} &= y_i^k + \Delta y \left[s_i^k | \hat{y}_{out}(s_i^{k-1}) \right] \\
t_i^{k+1} &= t_i^k + \tau \left[s_i^k | \hat{y}_{out}(s_i^{k-1}) \right]
\end{aligned} \tag{5}
$$

where both y_i^{k+1} and τ_i^{k+1} are determined through a Markov chain, which is related to the transverse location assigned to the particle in the periodic cell

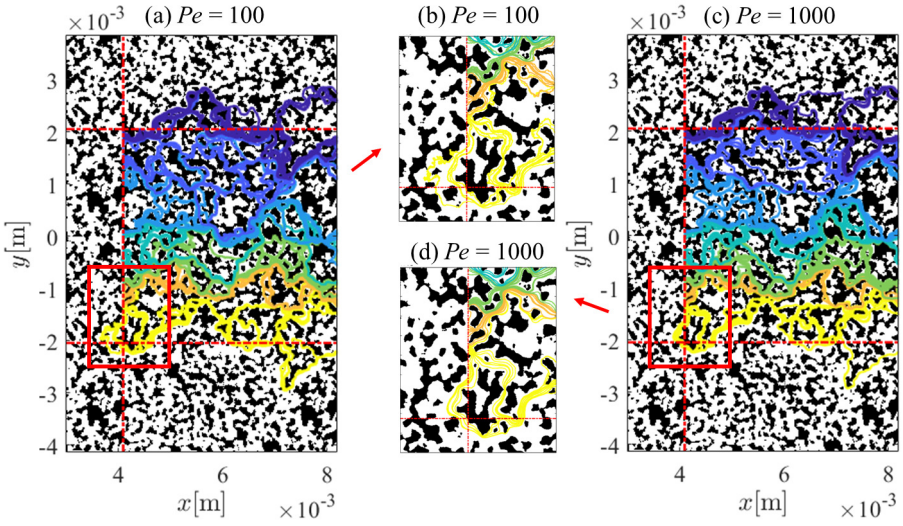

Figure 2: Sample of 100 trajectories employed for model parameterization for (a), (b) $Pe = 100$ and (c), (d) $Pe = 1000$, dashed red lines indicate the unit cell boundaries, the trajectories are binned in different colours as a function of the y_{in} location. The two middle panels represent a zoom on the region highlighted in red for the two cases.

during successive steps k, leveraging the information given by the trajectories in s_i. The innovative feature of the model in Eq. (5) with respect to previous implementations [30, 21] is that it allows for predictions of transverse spreading over successive Markov steps. This is achieved by considering y as a continuous variable, i.e., the Markov chain has a longitudinal fixed spatial step L_x while transport along y is considered through the $\Delta y(s_i)$ obtained from the trajectories s_i recorded during the parameterization stage. In essence, at the beginning of the simulation (step $k = 0$) each particle i is assigned to an initial location y_i^0 corresponding to a selected initial or boundary condition (e.g., flux weighted or uniform distribution on the inlet boundary). From this information we select a trajectory s_i^1, randomly sampling from those whose $y_{in}(s_i)$ lies in the same bin interval as y_i^0. By selecting the trajectory

we also obtain a given travel time $\tau(s_i^1)$ and transverse displacement $\Delta y(s_i^1)$, from which we evaluate $\hat{y}_{out}(s_i^1)$. The latter can be then used to select a new trajectory s_i^2 for the next transition and the procedure can then be repeated for any arbitrary step number $k > 0$.

2.3. Model outputs

To analyze the outputs of our tSMM model, our analysis relies on the following dimensionless space-time coordinates

$$\tilde{x} = \frac{x^k}{L}, \qquad \tilde{y} = \frac{y_c}{L}, \qquad \tilde{t} = \frac{tU}{L} \tag{6}$$

where $L = L_x = L_y$, x^k corresponds to the longitudinal spatial coordinate of k^{th} Markov step (see Eq. (5)) and $y_c(x) = y(x) - \overline{y}(x)$, i.e., is the transverse location centered with respect to the average transverse position $\overline{y}(x)$ observed at a given x. The value of $\overline{y}(x)$ is not constant with x because the average transverse velocity component is not exactly equal to zero. While this component is only approximately 1% of the longitudinal mean velocity U, it still induces plume migration along y after a number of cells.

The key output of the tSMM is the joint probability distribution $P(\tilde{x}, \tilde{y}, \tilde{t})$. In this distribution, the variable $\tilde{x}$ can only assume discrete values, while the $\tilde{y}, \tilde{t}$ are continuous.

Physically meaningful information related to the plume can then be extracted from this joint probability by considering conditional and marginal distributions. In our analysis we will consider the conditional distributions $P(\tilde{t}, \tilde{y}|\tilde{x})$ for a given dimensionless downstream distance $\tilde{x}$, or $P(\tilde{x}, \tilde{y}|\tilde{t})$ for a given dimensionless time, $\tilde{t}$. Examples of these conditional distributions

$P(\tilde{t}, \tilde{y}|\tilde{x})$ for $\tilde{x} = 5$, 10, 25 and 50 and $P(\tilde{x}, \tilde{y}|\tilde{t})$ for $\tilde{t} = 20$, obtained from the tSMM are shown in Figure 3a and b for $Pe = 100$ and 1000, respectively.

In addition, we consider the marginal probability distributions $P(\tilde{x}, \tilde{y})$, and $P(\tilde{t}|\tilde{x})$, $P(\tilde{y}|\tilde{x})$ conditional to a given dimensionless downstream distance. These distributions have a clear physical meaning: the marginal distribution $P(\tilde{x}, \tilde{y})$ represents the steady state distribution of the particle plume, while $P(\tilde{t}|\tilde{x})$ corresponds to the breakthrough curve, i.e., the first passage time probability distribution at distance $\tilde{x}$. Finally, the probability distribution $P(\tilde{y}|\tilde{x})$ provides the probability distribution associated with transverse position at a control plane and is related solely to transport in the transverse direction.

To produce benchmark data against which to test the tSMM we run a 50 cell high resolution random walk direct numerical simulation (DNS) using transport Eq. (3). The accuracy of the tSMM defined in section 2.2 will be tested by comparing the above mentioned probability distributions with their analogs obtained from the DNS. For each of the above defined distributions we provide a quantitative evaluation of the mismatch between DNS and tSMM using the Hellinger distance [35]

$$HD[F_1, F_2] = \frac{1}{\sqrt{2}} \sqrt{\sum_{i=1}^{N} \left(\sqrt{f_{1,i}} - \sqrt{f_{2,i}} \right)^2} \tag{7}$$

where F_1 is any of the above-mentioned marginal or conditional distributions predicted by DNS and F_2 corresponds to its counterpart obtained with the tSMM. These distributions are approximated through N discrete bins and $f_{1,i}$, $f_{2,i}$ are the values of the distributions in the i^{th} bin.

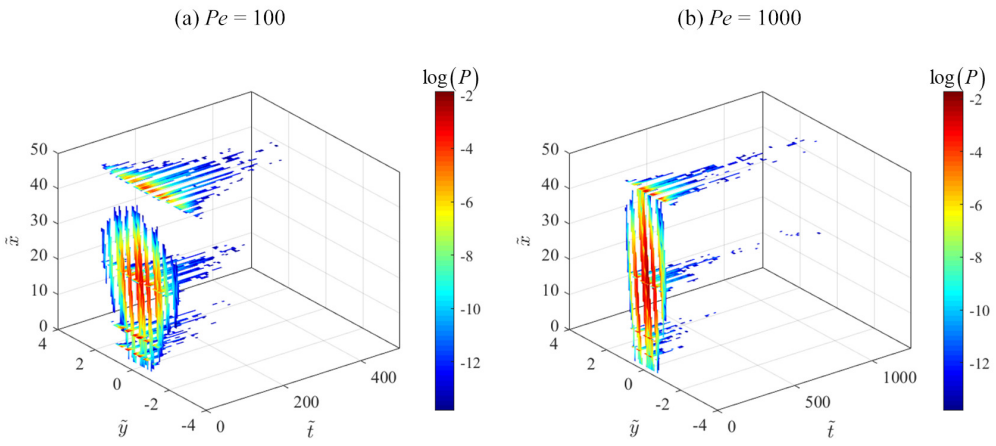

Figure 3: Conditional joint distributions $P(\tilde{t}, \tilde{y}|\tilde{x})$ for $\tilde{x} = 5$, 10, 25, 50 and $P(\tilde{x}, \tilde{y}|\tilde{t})$ for $\tilde{t} = 20$ predicted by the tSMM considering (a) $Pe = 100$ and (b) $Pe = 1000$

The HD metric quantifies the distance between two probability measures and it is a proper distance metric in the mathematical sense, by satisfying the properties of non-negativity, symmetry, and triangle inequality. HD is also bounded between 0 and 1, where 0 means that the two distributions are indiscernible and 1 that they are maximally distant.

3. Results

First we show results obtained considering parameterization of the tSMM with $N_s = 10^6$, $N_B = 100$, $dt^* = 10^{-5}$ s and 10^{-6} s for $Pe = 100$ and $Pe = 1000$, respectively. The time step dt^* indicates the values of dt evaluated according to Eq. (4). Then, in section 3.3 we analyze the impact of parameters N_B and dt on the accuracy of the tSMM. For all cases, including the DNS reference simulation and tSMM, we impose a flux weighted boundary conditions. Note that In the reference DNS simulation the dt parameter is kept constant and equal to dt^*.

3.1. Model performance as a function of Pe

The tSMM is able to replicate the shape of the reference conditional distribution $P(\tilde{t}, \tilde{y}|\tilde{x})$ obtained from the DNS for both investigated Péclet numbers. Figure 4a shows the joint distribution $P(\tilde{t}, \tilde{y}|\tilde{x})$ for $\tilde{x} = 25$ and $Pe = 100$ from the high resolution direct numerical simulations and corresponding results obtained with the tSMM (Figure 4b). The agreement between the two solutions is significant for all transverse coordinates, $\tilde{y}$, and dimensionless travel times, $\tilde{t}$. Analogous results are obtained for $Pe = 1000$ (see Figure 4c and d) and for all other investigated Markov steps (not shown). For both Pe values the maximum value of the probability distributions is found at $\tilde{y} \approx 0$. Note that $\tilde{y}$ locations associated with zero probability across the whole time window correspond to the occurrence of solid along the considered transverse section.

To quantify the accuracy of the tSMM outputs with respect to the reference DNS, Figure 5 shows the metric $HD[P_{DNS}(\tilde{y}, \tilde{t}|\tilde{x}); P_{tSMM}(\tilde{y}, \tilde{t}|\tilde{x})]$ defined in Eq. (7) for both investigated Pe numbers and all Markov steps. We note that the distance between the DNS and the tSMM distributions slightly increases with $\tilde{x}$ and is generally larger for $Pe = 100$ than for $Pe = 1000$. This result is likely due to the fact that the effect of noise in low probability values increases with the strength of diffusion.

Figure 6 depicts conditional joint distribution $P(\tilde{x}, \tilde{y}|\tilde{t})$ for $\tilde{t} = 20$, corresponding to the time dependent solute plume. DNS and tSMM predictions are shown for $Pe = 100$ (see Figure 6a, b) and for $Pe = 1000$ (see Figure 6c, d). Again, the tSMM is able to capture all essential features displayed by the fully resolved simulations. Note that tSMM allows for predictions

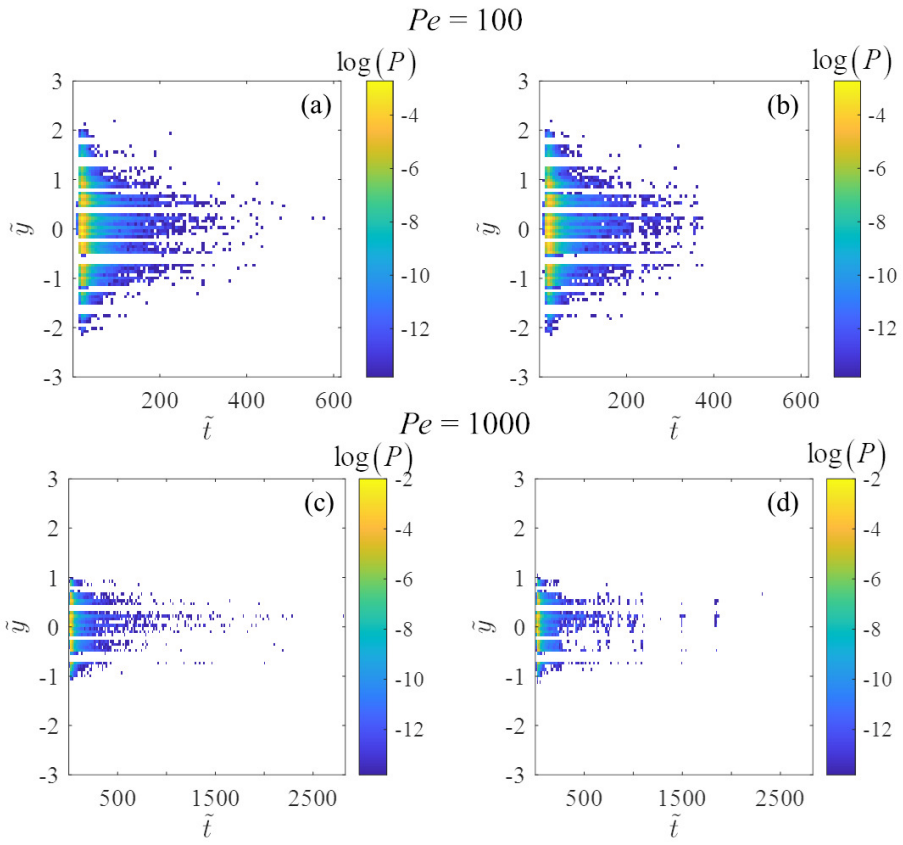

Figure 4: Conditional joint distributions $P(\tilde{t}, \tilde{y}|\tilde{x})$ for $\tilde{x} = 25$ and $Pe = 100$ obtained with (a) DNS, (b) tSMM and for $Pe = 1000$ predicted by (c) DNS and (d) tSMM.

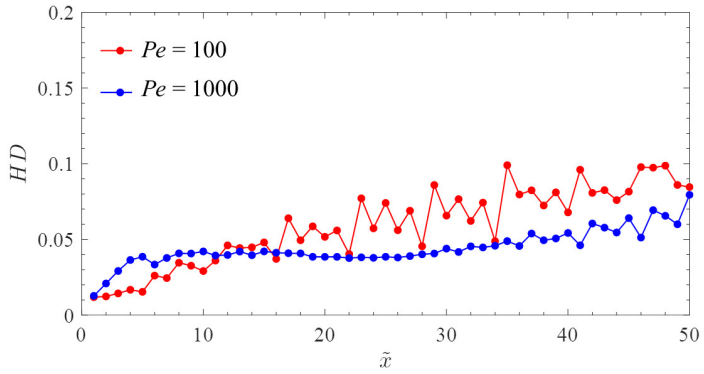

Figure 5: $HD[P_{DNS}(\tilde{y},\tilde{t}|\tilde{x}); P_{tSMM}(\tilde{y},\tilde{t}|\tilde{x})]$ as a function of the downstream location $\tilde{x}$ for $Pe = 100$ (red) and 1000 (blue).

of the evolution of the plume in the longitudinal and transverse directions employing a significantly smaller computational effort than the DNS. As an example, the computational time for running the tSMM is approximately 1% of that one needed for the DNS results when considering 50 Markov steps. Note that this percentage decreases for simulation across higher numbers of unit cells (i.e., the computational gain increases with the dimension of the system of interest).

The marginal distributions $P(\tilde{x},\tilde{y})$ are depicted in Figure 7a and b for $Pe = 100$ and 1000 respectively. As mentioned above, these distributions identify the steady-state plume for a nonreactive solute. These distributions are here obtained at no additional computational cost with respect to the transient case, which for a DNS would not be the case and significant additional cost would be required.

Figure 8 displays breakthrough curves $P(\tilde{t}|\tilde{x})$ considering travel distances $\tilde{x} = 5$, 10, 25 and 50 from the injection location and provides a quantitative comparison between the reference DNS and the tSMM results. We note that

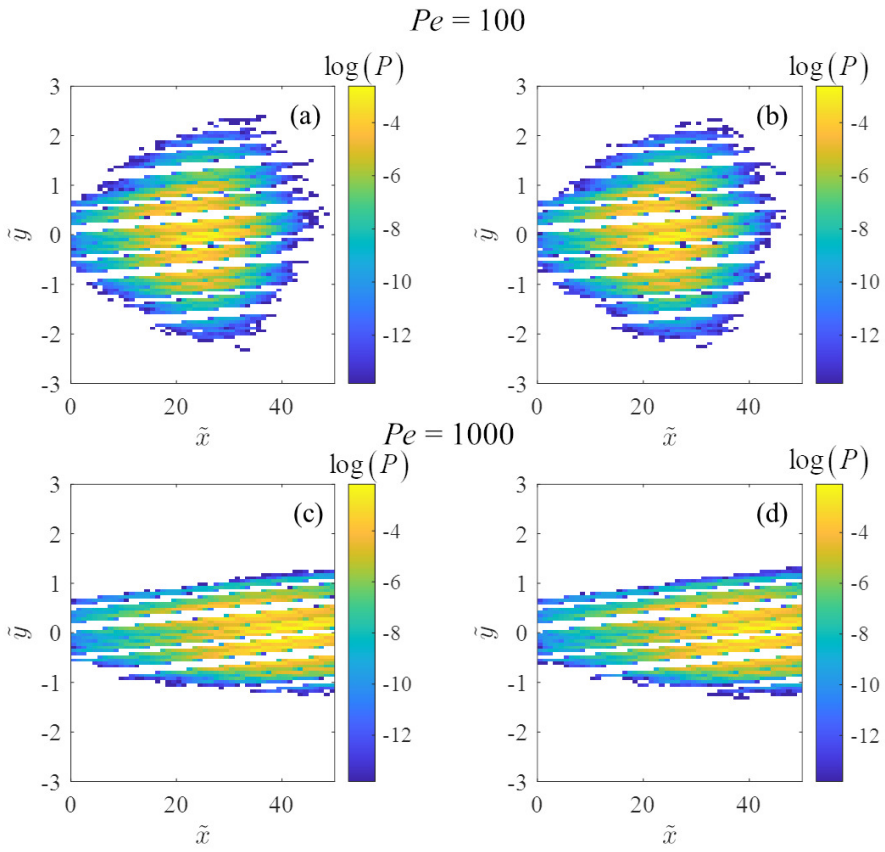

Figure 6: Conditional distributions $P(\tilde{x}, \tilde{y}|\tilde{t})$ for $\tilde{t} = 20$ and $Pe = 100$ obtained with (a) DNS (b) tSMM and for $Pe = 1000$ predicted by (c) DNS and (d) tSMM

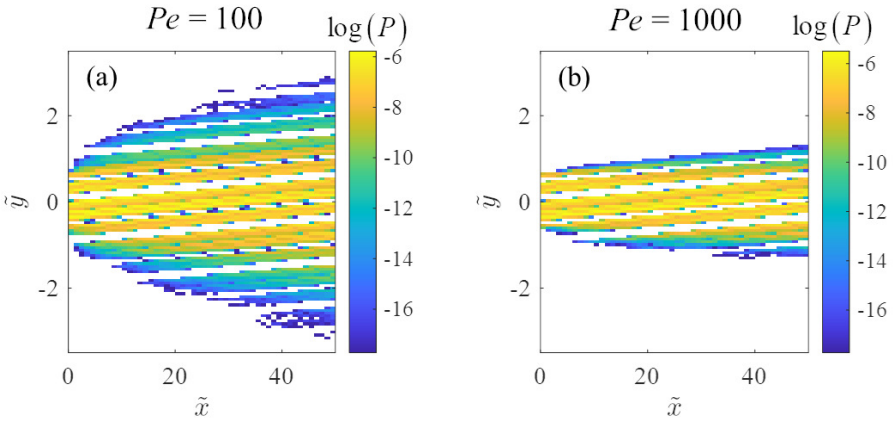

Figure 7: Marginal distribution $P(\tilde{x}, \tilde{y})$ for (a) $Pe = 100$ and (b) $Pe = 1000$.

the tSMM can reproduce the breakthrough curves across a wide range of distances and both Péclet numbers. This result shows that the trajectory-based upscaled model accurately predicts arrival times in a porous medium made of periodic unit cells displaying a disordered geometry and is in line with those obtained within simpler geometrical settings [30].

The comparison between tSMM and DNS marginal distribution of transverse locations $P(\tilde{y}|\tilde{x})$ is shown in Figure 9 for two selected distances from the injection ($\tilde{x} = 5$ and $\tilde{x} = 25$) and for both investigated Pe numbers. To compare the spreading of the particle plume over all Markov steps we consider the standard deviation of distribution $P(\tilde{y}|\tilde{x})$ as a function of $\tilde{x}$ (see Figure 10).

Results obtained through the tSMM are in close agreement with those yielded by the DNS. We observe that the change in Pe has marked effects on transverse spreading of the solute, as has been previously observed in laboratory and numerical studies [10, 13]. In particular, the standard deviation σ_y

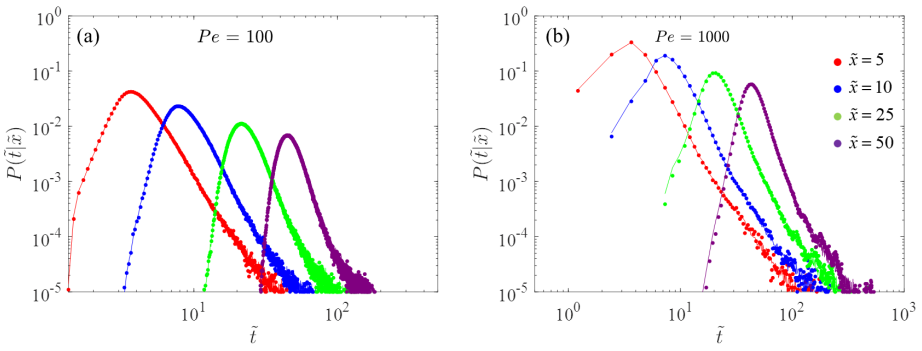

Figure 8: Breakthrough curves $P(\tilde{t}|\tilde{x})$ obtained at control planes located at distances $\tilde{x} = 5, 10, 25, 50$ unit cells for (a) $Pe = 100$ and (b) $Pe = 1000$. Symbols and lines represent the DNS and tSMM results, respectively.

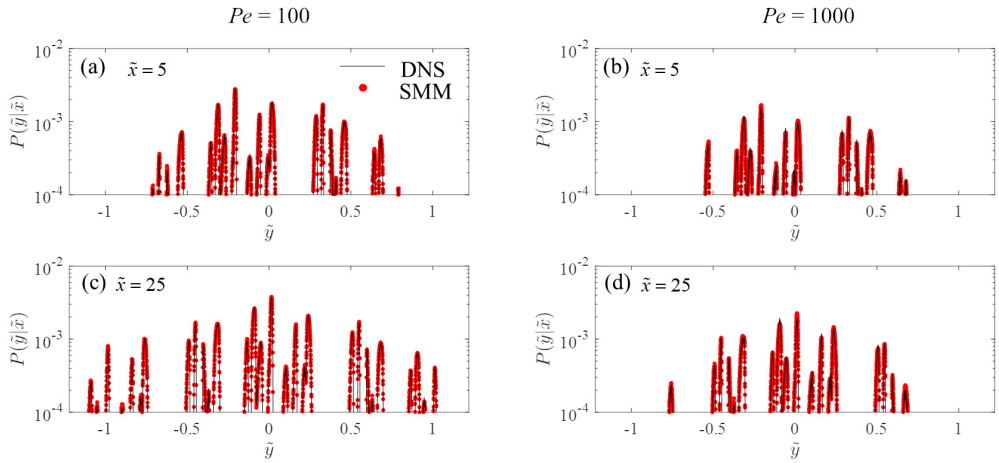

Figure 9: Comparison between the marginal distributions $P(\tilde{y}|\tilde{x})$ as given by direct numerical simulation (black lines) and tSMM (red dots) for $\tilde{x} = 5$ and a) $Pe = 100$, b) $Pe = 1000$, for $\tilde{x} = 25$ and c) $Pe = 100$ and d) $Pe = 1000$.

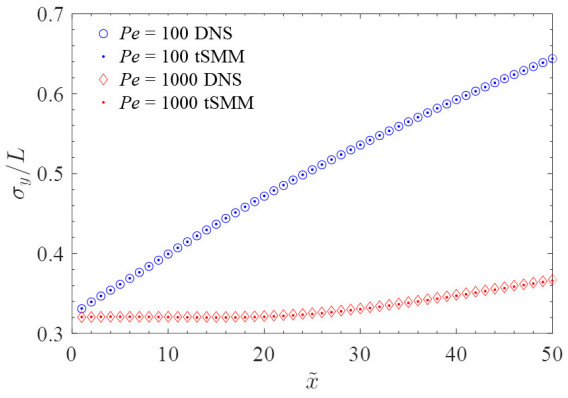

Figure 10: Comparison of the standard deviation, σ_y, of the distribution $P(\tilde{y}|\tilde{x})$ for the DNS and tSMM as a function of $\tilde{x}$.

continuously increases as a function of the longitudinal distance traveled for $Pe = 100$. On the contrary, σ_y is approximately constant up to $\tilde{x} = 20$ for $Pe = 1000$ and then starts increasing. This result implies that for such an advection-dominated situation we only observe significant transverse spreading after particles have traveled a distance of 20 cells. This result is due to the converging-diverging nature of advective streamlines in two-dimensional fields, and this particular behavior might be different if investigated in three-dimensions. Yet, the tSMM is able to predict these different dynamics based on the simulation of transport across a single unit cell. Note also that the methodology can extended to three dimensions, upon relying on the same procedure described in Section 2.2.

3.2. Steady state plumes with first order degradation

As a showcase application of the capabilities of the tSMM, we also evaluate the influence of a first order reaction on pinching off the steady-state plume. We assume in this application that the solute undergoes degrada-

tion following linear kinetics. This is accounted for in a straightforward manner in the tSMM framework. Starting from the conservative plume results (see Figure 7), for each particle we define the probability of reaction as $R_i(t,\lambda) = 1 - e^{-\lambda t}$, where λ is the kinetic degradation rate. Then we compare R_i with a random number, U_i, drawn from a standard uniform distribution. If $U_i \geqslant P_i$ no reaction occurs while if $U_i < P_i$ the particle is removed from the system. In our examples λ is chosen based on obtaining specific values of Damkhöler numbers, $Da = \frac{\ell_S^2 \lambda}{D}$.

We compute marginal distributions $P(\tilde{x}, \tilde{y})$ to represent the steady state plume for this reactive scenario. The results obtained for $Da = 1$ and 5 (corresponding to $\lambda = 0.1$ and 0.5) and $Pe = 100$ are depicted in Figures 11a and b while Figures 11c and d show the case associated with $Da = 5$ and 10 (corresponding to $\lambda = 0.5$ and 1) and $Pe = 1000$. These results portray the ability of our proposed tSMM to predict transport in longitudinal and transverse direction while also accounting for a reactive solute undergoing a first order reaction process. Note that the results are obtained at negligible additional computational cost with respect to the unsteady state, conservative, transport simulations.

3.3. Error analysis

To provide a quantitative description of the influence of parameters N_B and dt on the accuracy of the proposed spatial Markov model we evaluate $HD[F_1, F_2]$, see Eq. 7, choosing as F_1 and F_2 the marginal distributions of travel times, $P(\tilde{t}|\tilde{x})$, or transverse positions, $P(\tilde{y}|\tilde{x})$, conditional to a given downstream location $\tilde{x}$ from the injection point, evaluated with DNS and tSMM respectively. Note that the time step is kept constant and equal to

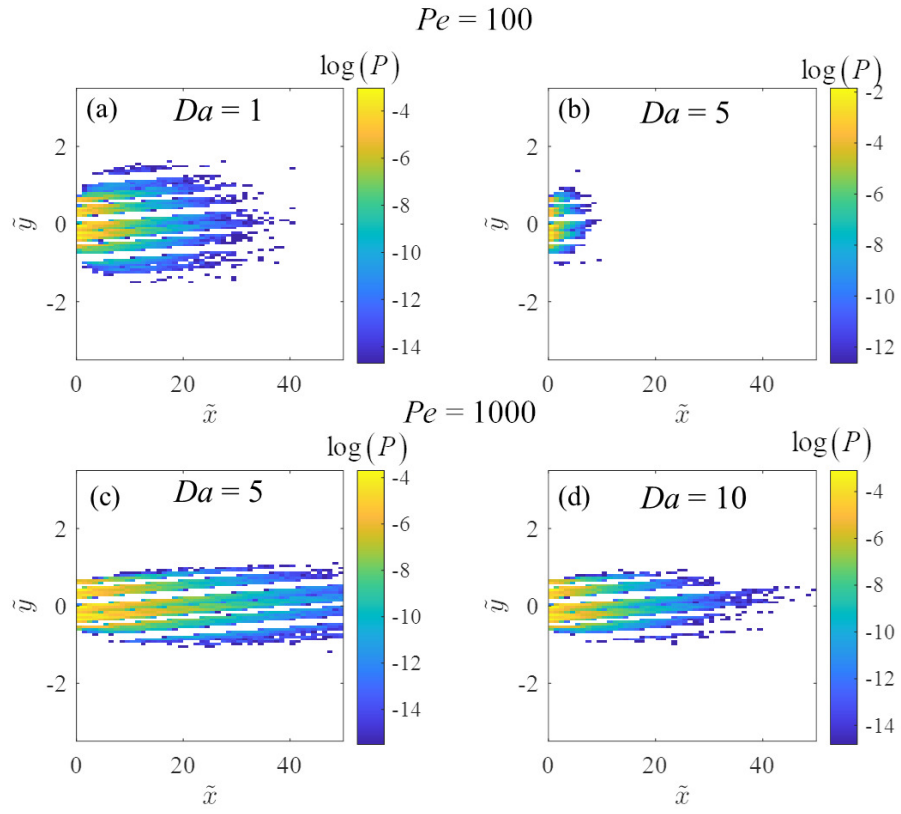

Figure 11: Marginal distribution $P(\tilde{x}, \tilde{y})$ for a reactive contaminant undergoing a degradation following a linear kinetics for $Pe = 100$ (a) $Da = 1$, (b) $Da = 5$, and $Pe = 1000$ (c) $Da = 5$, (d) $Da = 10$.

dt^* in the DNS, while we consider in following different values for the simulation of the trajectories employed to parameterize the tSMM, To simplify the notation we introduce here the following indicators

$$HD_t = HD[P_{DNS}(\tilde{t}|\tilde{x}); P_{SMM}(\tilde{t}|\tilde{x})] \tag{8}$$

$$HD_y = HD[P_{DNS}(\tilde{y}|\tilde{x}); P_{SMM}(\tilde{y}|\tilde{x})] \tag{9}$$

to assess the model errors. The analysis is performed considering both $Pe = 100$ and $Pe = 1000$ and considering different values of N_B and dt for the parameterization of the tSMM, while, as mentioned above, in the reference DNS the dt is constant and equal to dt^*. In order to provide an overall assessment of the impact of parameters dt and N_B we focus on the average of HD_α (with $\alpha = t, y$) across all 50 investigated Markov steps (the averaging operator is denoted by the symbol $\langle\cdot\rangle$). Figures 12a and b show $\langle HD_t\rangle$ and $\langle HD_y\rangle$ as a function of dt/dt^* and N_B, respectively. Continuous lines correspond to $Pe = 100$, while dashed lines depict results associated with $Pe = 1000$. Red and blue colors are related to arrival time and transverse location distributions, respectively. Note that for $Pe = 100$ both $\langle HD_t\rangle$ and $\langle HD_y\rangle$ are not very sensitive to the choice of parameter dt (see Figure12a). On the contrary for $Pe = 1000$ we observe a sharp increase of $\langle HD_t\rangle$ and $\langle HD_y\rangle$ for $dt > 2dt^*$. This is probably due to the fact that advective particle displacements depend linearly on dt, as opposed to the diffusive ones which scale with $dt^{0.5}$. The variation of $\langle HD_t\rangle$ and $\langle HD_y\rangle$ as a function of N_B are displayed in Figure 12b for the two investigated Pe numbers. These results show that the quality of model predictions deteriorates for decreasing num-

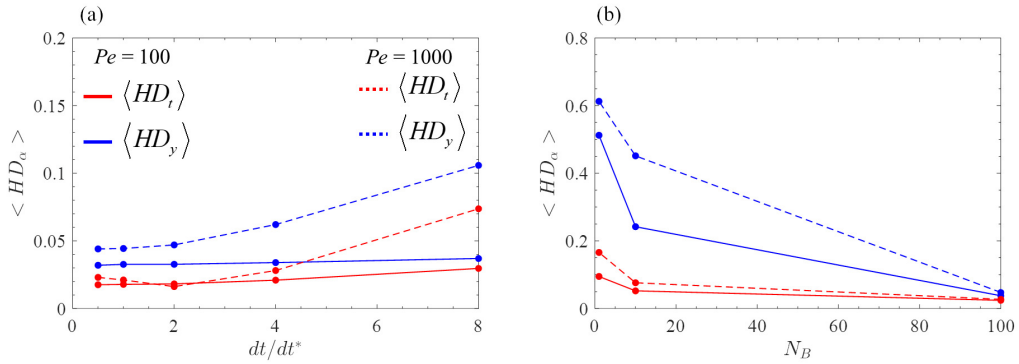

Figure 12: $\langle HD_\alpha \rangle$ for $Pe = 100$ and $Pe = 1000$ as a function of the Markov step number (cell number) for different dt and numbers of bins N_B employed in the parameterization step.

ber of bins associated with the tSMM parameterization. Note that $N_B = 1$ corresponds to considering the particle trajectories as totally uncorrelated across successive Markov steps, while setting $N_B > 1$ in the tSMM parameterization allows consideration of correlation between particle trajectories belonging to the same bin. We note that considering uncorrelated particle trajectories does not provide good agreement between DNS and tSMM distributions, as indicated by high values of the HD_α metrics. Also in this case correlation effects at a fixed downstream distance become stronger as Péclet number increases, in line with the results of previous studies [22, 31].

4. Discussion and conclusions

Our study proposes a methodology for upscaling solute plumes in periodic porous media through a trajectory based spatial Markov Model. We extend the work of [30] to the case of a multi-dimensional unsteady solute transport and exemplify our approach considering a two-dimensional porous medium with a disordered geometry. Our framework is based on the simula-

tion of advection-diffusion random walk particle trajectories across a single periodic flow cell with the aim of predicting transport over a much larger scale. In particular, our analysis explicitly includes the evaluation of the joint space-time probability distributions associated with solute plumes providing an efficient and accurate representation of both transient and steady state transport in porous media for different Pe numbers. Our work leads to the following major conclusions:

1. From a comparison with high resolution direct numerical simulations we show that the proposed tSMM accurately predicts spatial and temporal distributions of a conservative solute plume using information collected from a single cell simulation. The current framework is not restricted to a simplified geometry setting or a particular flow condition, but can be employed to accurately predict multi-dimensional transport in a realistic two-dimensional pore space once the flow field has been evaluated. Note that, in principle our methodology can be used with different type of initial injection condition, e.g. flux-weighted or uniformly distributed, pulse or continuous injection, and can be extended to a three-dimensional setup.
2. Our model is able to predict different transport dynamics, particularly regarding the influence of Pe on transverse plume spreading. Our results are in line with previous laboratory and numerical studies [10, 13]. In particular, the change in Pe, due to a change in the diffusion coefficient of the compound, had marked effects on transverse spreading of the solute and this is well captured by our upscaling approach.
3. Particle trajectories and associated travel times, which were simulated

with the proposed tSMM to predict conservative transport, can be naturally extended to simulate reactive transport processes with negligible additional computational cost. As an example, in this work we analyse the influence of a first order kinetic reaction on a steady state plume. To do so our model has been coupled with a probabilistic representation of a linear degradation reaction and applied for several Da numbers. Note that the methodology is already fully compatible with the analysis of other types of reactions (e.g. sorption/desorption) as was shown by [31] for an idealized benchmark problem.

4. The effect of tSMM parameterization (in particular the parameters dt and N_B) was studied for the two analysed Pe. As expected, the difference between tSMM and DNS distribution both in space and time increases with increasing dt and decreasing N_B respectively. A marked effect of parameterization was observed for $Pe = 1000$ with respect to $Pe = 100$ due to fact that (i) the contribution of the advective transport, which increases with Pe, is more affected by the choice of dt employed in the tSMM parameterizazion and (ii) the relevance of particle trajectory correlation increases with Pe.

For all the above points the simulation time needed for the tSMM is negligible if compared to the one required for high resolution direct numerical simulation. This is one of the great advantages of the proposed tSMM which allows predicts of multi-dimensional transport across large distances (for both conservative and reactive solutes) without the burden of excessive computational resources. Note that, in its current form, the model can be applied to a spatially periodic domain. This restriction is similar to the fact that

solving a closure problem on a periodic unit cell is required for many well established upscaling procedures. At the same time, broadening the scenarios of interest, for example extending the methodology to upscaling transport of a conservative and/or reactive solute in a disordered non periodic porous domain would constitute additional elements of interest which are compatible with the approach we rest upon. A first attempt in this direction has been provided by [21, 36] obtaining promising results which can be advanced in the context of future investigations.

Acknowledgments

Data Availability Statement

Data sets for this research are available online at
https://data.mendeley.com/datasets/rzg53tn963/draft

References

[1] A. Scheidegger, Statistical hydrodynamics in porous media, Journal of Applied Physics 25 (8) (1954) 994–1001. doi:10.1063/1.1721815.

[2] A. H.-D. Cheng, J. Bear, Modeling Groundwater Flow and Contaminant Transport, Springer Publishing Company, 2016.

[3] F. Valdés-Parada, D. Lasseux, F. Bellet, A new formulation of the dispersion tensor in homogeneous porous media, Advances in Water Resources 90 (2016) 70–82. doi:10.1016/j.advwatres.2016.02.012.

[4] J. Salles, J.-F. Thovert, R. Delannay, L. Prevors, J.-L. Auriault, P. Adler, Taylor dispersion in porous media. determination of the dispersion tensor, Physics of Fluids A 5 (10) (1992) 2348–2376.

[5] B. Berkowitz, A. Cortis, M. Dentz, H. Scher, Modeling non-fickian transport in geological formations as a continuous time random walk, Rev. Geophys. 44 (2).

[6] B. Wood, F. Valdés-Parada, Volume averaging: Local and nonlocal closures using a green's function approach, Advances in Water Resources 51 (2013) 139–167. doi:10.1016/j.advwatres.2012.06.008.

[7] Y. Davit, B. D. Wood, G. Debenest, M. Quintard, Correspondence between one-and two-equation models for solute transport in two-region heterogeneous porous media, Transport in porous media 95 (1) (2012) 213–238.

[8] G. Porta, G. Ceriotti, J.-F. Thovert, Comparative assessment of continuum-scale models of bimolecular reactive transport in porous media under pre-asymptotic conditions, Journal of contaminant hydrology 185 (2016) 1–13.

[9] O. Cirpka, A. Valocchi, Two-dimensional concentration distribution for mixing-controlled bioreactive transport in steady state, Advances in Water Resources 30 (6-7) (2007) 1668–1679. doi:10.1016/j.advwatres.2006.05.022.

[10] G. Chiogna, C. Eberhardt, P. Grathwohl, O. Cirpka, M. Rolle, Evidence of compound-dependent hydrodynamic and mechanical transverse dispersion by multitracer laboratory experiments, Environmental Science and Technology 44 (2) (2010) 688–693. doi:10.1021/es9023964.

[11] Y. Tang, C. Werth, R. Sanford, R. Singh, K. Michelson, M. Nobu, W.-T. Liu, A. Valocchi, Immobilization of selenite via two parallel pathways during in situ bioremediation, Environmental Science and Technology 49 (7) (2015) 4543–4550. doi:10.1021/es506107r.

[12] T. Willingham, C. Werth, A. Valocchi, Evaluation of the effects of porous media structure on mixing-controlled reactions using pore-scale modeling and micromodel experiments, Environmental Science and Technology 42 (9) (2008) 3185–3193. doi:10.1021/es7022835.

[13] M. Rolle, D. Hochstetler, G. Chiogna, P. K. Kitanidis, P. Grathwohl, Experimental investigation and pore-scale modeling interpretation of compound-specific transverse dispersion in porous media, Transport in

Porous Media 93 (3) (2012) 347–362. doi:https://doi.org/10.1016/j.advwatres.2020.103574.

[14] M. Muniruzzaman, M. Rolle, Impact of multicomponent ionic transport on ph fronts propagation in saturated porous media, Water Resources Research 51 (8) (2015) 6739–6755. doi:10.1002/2015WR017134.

[15] Y. Ye, G. Chiogna, O. Cirpka, P. Grathwohl, M. Rolle, Experimental investigation of transverse mixing in porous media under helical flow conditions, Physical Review E 94 (1). doi:10.1103/PhysRevE.94.013113.

[16] J.-L. Auriault, C. Moyne, H. Souto, On the asymmetry of the dispersion tensor in porous media, Transport in Porous Media 85 (3) (2010) 771–783. doi:10.1007/s11242-010-9591-y.

[17] S. Pride, D. Vasco, E. Flekkoy, R. Holtzman, Dispersive transport and symmetry of the dispersion tensor in porous media, Physical Review E 95 (4). doi:10.1103/PhysRevE.95.043103.

[18] T. Le Borgne, D. Bolster, M. Dentz, P. Anna, A. Tartakovsky, Effective pore-scale dispersion upscaling with a correlated continuous time random walk approach, Water Resources Research 47 (12) (2011) W12538.

[19] P. K. Kang, P. Anna, J. P. Nunes, B. Bijeljic, M. J. Blunt, R. Juanes, Pore-scale intermittent velocity structure underpinning anomalous transport through 3-d porous media, Geophysical Research Letters 41 (17) (2014) 6184–6190.

[20] A. Puyguiraud, P. Gouze, M. Dentz, Stochastic dynamics of lagrangian

pore-scale velocities in three-dimensional porous media, Water Resources Researchdoi:10.1029/2018WR023702.

[21] T. Sherman, E. B. Janetti, G. R. Guédon, G. Porta, D. Bolster, Upscaling transport of a sorbing solute in disordered non periodic porous domains, Advances in Water Resources (2020) 103574doi:https://doi.org/10.1016/j.advwatres.2020.103574.

[22] D. Bolster, Y. Méheust, T. Le Borgne, J. Bouquain, P. Davy, Modeling preasymptotic transport in flows with significant inertial and trapping effects–the importance of velocity correlations and a spatial markov model, Advances Water Resources 70 (2014) 89–103.

[23] T. Sherman, A. Foster, D. Bolster, K. Singha, Predicting downstream concentration histories from upstream data in column experiments, Water Resources Research (2018) 9684–9694.

[24] A. Russian, M. Dentz, P. Gouze, Time domain random walks for hydrodynamic transport in heterogeneous media, Water Resources Research 52 (5) (2016) 3309–3323. doi:10.1002/2015WR018511.

[25] E. Wright, N. Sund, D. Richter, G. Porta, D. Bolster, Upscaling mixing in highly heterogeneous porous media via a spatial markov model, Water 11 (1) (2019) 53.

[26] M. Schmuck, P. Berg, Effective macroscopic equations for species transport and reactions in porous catalyst layers, Journal of the Electrochemical Society 161 (8) (2014) E3323–E3327. doi:10.1149/2.037408jes.

[27] H. Kim, J. Bae, D. Choi, An analysis for a molten carbonate fuel cell of complex geometry using three-dimensional transport equations with electrochemical reactions, International Journal of Hydrogen Energy 38 (11) (2013) 4782–4791. doi:10.1016/j.ijhydene.2013.01.061.

[28] T. Gebäck, A. Heintz, A pore scale model for osmotic flow: Homogenization and lattice boltzmann simulations, Transport in Porous Media 126 (1) (2019) 161–176. doi:10.1007/s11242-017-0975-0.

[29] F. Municchi, M. Icardi, Macroscopic models for filtration and heterogeneous reactions in porous media, Advances in Water Resources 141 (2020) 103605. doi:https://doi.org/10.1016/j.advwatres.2020.103605.

[30] N. L. Sund, G. M. Porta, D. Bolster, Upscaling of dilution and mixing using a trajectory based spatial markov random walk model in a periodic flow domain, Advances in Water Resources 103 (2017) 76–85.

[31] T. Sherman, A. Paster, G. Porta, D. Bolster, A spatial markov model for upscaling transport of adsorbing-desorbing solutes, Journal of contaminant hydrology 222 (2019) 31–40.

[32] P. K. Smolarkiewicz, C. L. Winter, Pores resolving simulation of Darcy flows, Journal of Computational Physics 229 (9) (2010) 3121–3133.

[33] J. D. Hyman, C. L. Winter, Stochastic generation of explicit pore structures by thresholding Gaussian random fields, Journal of Computational Physics 277 (2014) 16–31.

[34] OpenCFD Limited, OpenFOAM The Open Source CFD Toolbox, user guide version v1712, https://www.openfoam.com/, accessed: 2019-09-29 (2017).

[35] E. Hellinger, Neue begrundung der theorie quadratischer formen von unendlichvielen veränderlichen., Journal Für Die Reine Und Angewandte Mathematik (1909) 210–271doi:10.1515/crll.1909.136.210.

[36] T. Sherman, J. Hyman, M. Dentz, D. Bolster, Characterizing the influence of fracture density on network scale transport, Journal of Geophysical Research: Solid Earth 125 (1) (2020) e2019JB018547.